Limits to flow detection in pulsed gradient spin echo NMR

Nathan H. Williamson[a,b,*], Michal E. Komlosh[b,c], Dan Benjamini[b,c], Peter J. Basser[b]

[a]National Institute of General Medical Sciences, National Institutes of Health, Bethesda, MD, USA
[b]Eunice Kennedy Shriver National Institute of Child Health and Human Development, National Institutes of Health, Bethesda, MD, USA
[c]The Center for Neuroscience and Regenerative Medicine, Uniformed Service University of the Health Sciences, Bethesda, MD, USA

Abstract

Velocity detection with single pulsed gradient spin echo (PGSE) NMR is known to be limited by diffusion smearing the phase coherence and obscuring dispersive attenuation. We present an equation for the lowest detectable velocity with phase contrast velocimetry which incorporates the signal-to-noise ratio. We show how to best sample q-space when approaching this limit. We confirm that the apparent diffusion/dispersion coefficient can be used to infer fluid velocity for Péclet number $Pé > 1$. When measuring flow in biological systems we determined that with realistic experimental protocols the limits are roughly 1 $\mu m/s$ for velocimetry and 300 $\mu m/s$ for diffusometry.

Keywords:
Pulsed field gradient (PFG)
Phase contrast velocimetry
Self-diffusion
Diffusion tensor imaging (DTI)
q-space imaging
Dispersion
Intra voxel incoherent motion (IVIM)
Glymphatic system
magnetic resonance in porous media

1. Introduction

A single pair of magnetic gradient pulses provides sensitivity to flow through both the signal phase shift and signal attenuation [1]. The phase shift measures the mean velocity of spins within the excited region. Attenuation measures the enhanced mixing and spreading in space due to incoherent motion. The lowest detectable velocity is limited by what coherence or additional attenuation can be observed in the presence of motion due to self-diffusion. Slow flows through the brain have recently been identified as part of a mechanism of waste clearance termed the glymphatic system [2]. Researchers have set out to measure these flows with pulsed gradient spin echo (PGSE) methods [3], however whether or not they can be measured has not yet been answered.

Callaghan discussed in rough terms the limit for phase contrast velocimetry [4], and Seymour and Callaghan provided a generalized approach for the measurement of flow and dispersion [5]. We build on these works to formulate quantitative limits for the lowest detectable velocities and to inform experimental parameter choices with single PGSE methods.

There is a strong interest to measure slow flows *in vivo*, e.g., measuring microcirculation of blood in capillary networks [6] and advective transport in the glymphatic system [7, 8]. Knowledge of the lower limit of velocity resolution, as well as how to best measure slow velocities with PGSE MRI may open the door for these and other new applications.

2. General Theory

One beautiful aspect of magnetic resonance is the multitude of information which can be encoded into its complex signal. Pulsed gradient spin echo (PGSE) NMR exemplifies this in the solution to the Bloch-Torrey equations for the normalized complex signal $E(q)$ arising from a fluid undergoing self-diffusion and coherent flow [9, 10, 11, 1],

$$E(q) = \exp\left(iqv\Delta - q^2 D\Delta\right), \tag{1}$$

in which q sensitizes the signal to displacement during an observation time Δ. With rectangular gradient pulse shapes of amplitude g and duration δ, in the case that $\delta << \Delta$, $q = \gamma g \delta$ where γ is the gyromagnetic ratio of the nuclei. Equation (1) shows that the phase shift between the real and imaginary channels and the attenuation of the signal intensity provide the ability to measure both mean coherent velocity, v, and random diffusion,

*Corresponding author: Nathan H. Williamson, E-mail: nathan.williamson@nih.gov
Email addresses: nathan.williamson@nih.gov (Nathan H. Williamson), peter.basser@nih.gov (Peter J. Basser)

D, using a single experiment. More generally, the signal describes the sum of the phase shifts associated with molecular displacements, Z, during Δ,

$$E(q,\Delta) = \int_{-\infty}^{\infty} \overline{P}(Z,\Delta)\exp(iqZ)dZ, \tag{2}$$

where $\overline{P}(Z,\Delta)$ is the average propagator [12]. In the case of diffusion and coherent flow, the propagator is a Gaussian with mean $v\Delta$ and standard deviation $\sqrt{2D\Delta}$,

$$\overline{P}(Z,\Delta) = (4\pi D\Delta)^{-1/2}\exp(-(Z-v\Delta)^2/(4D\Delta)), \tag{3}$$

and Eq. (2) becomes equivalent to Eq. (1). Advective (coherent) and dispersive (random) components of mass transport can both be measured with PGSE.

3. Phase contrast velocimetry

3.1. Background

Advection is measured from the PGSE signal phase shift [13]. This method is called phase contrast velocimetry [14]. When velocity displacements $v\Delta$ are similar to diffusive displacements $\sqrt{2D\Delta}$, the signal may attenuate with increasing q before showing a measurable phase shift. The minimum detectable velocity is therefore roughly

$$\langle v_{min}\rangle \approx \sqrt{\frac{2D}{\Delta}}. \tag{4}$$

Eq. (4) characterizes the "slow" flow regime.

Particularly slow flows have been imaged in plant systems, where water velocities between 10 and 100 μm/s have been imaged in wheat grain [15], in the phloem and xylem of plant stems [16, 17, 18], in individual giant algae cells [19], in living trees [20, 21], as well as in model soil with the goal of measuring water uptake by roots [22]. Velocimetry of industrially relevant systems involving slow flows include rocks [23, 24], microfluidics [25, 26, 27, 28], chromatography [29, 30], filtration [31, 32] and membrane biofouling [33], and catalytic reactors [34].

Plants and industrial systems often have preferential flow directions such that displacement encoding gradients and image resolution can be chosen accordingly. Measurement time is not usually limited, and full propagator measurements can be performed to separate mobile and immobile components as well as to obtain mean velocities. Certain systems, in particular mammalian ones, do not provide these luxuries. Likely for these reasons, as well as other confounding issues, velocimetry of animals has been limited to measuring fast flows. Soon after the first implementation of NMR velocity imaging in humans by Moran in 1982 [35], a number of clinical applications were found [36], including measuring cerebral [14, 37] and aortal [38, 39, 40, 41, 42] blood flow as well as cerebrospinal fluid (CSF) pulsation [43, 44].

Although by Eq. (4) displacements due to coherent flow scale with Δ and eventually become visible over displacements due to random motions that scale with $\sqrt{\Delta}$, it may not be possible to observe them until that point. The maximum Δ is limited by T_2 (for a spin echo) or T_1 (for a stimulated echo), and is typically somewhere in the window of 10 milliseconds to 1 second. For a gas, e.g., propane with $D \sim 10^{-6}$ m^2/s [45], $\langle v_{min}\rangle$ is on the order of 1 mm/s. Macromolecules and large particles can act as tracers and be sensitive to coherent displacements which are just larger than the particles themselves [46], e.g., for colloids with $D \sim 10^{-13}$ m^2/s [47] $\langle v_{min}\rangle \sim 100$ nm/s.

For free water, with $D = 2\times10^{-9}$ m^2/s and $\Delta = 1$ s, Eq. (4) predicts $\langle v_{min}\rangle \approx 60$ μm/s. However, Magdoom *et al.* recently measured velocities of water as slow as 1 μm/s [48] highlighting that Eq. (4) is only approximate. In practice, Eq. (4) can significantly over-estimates the true experimental $\langle v_{min}\rangle$. The main reason is because $\langle v_{min}\rangle$ is dependent on the signal to noise ratio (SNR). Wassenius and Callaghan derived $\langle v_{min}\rangle$ as the velocity determination error δv associated with finding the peak of a Gaussian propagator

$$\delta v = \sqrt{\frac{2D}{\Delta}\frac{\delta P}{A}}, \tag{5}$$

where $A/\delta P$ is the peak signal to rms noise ratio of the propagator [46]. Equation (2) shows that the propagator shares a Fourier relationship with the $E(q)$ signal. The spacing between points in the propagator domain share a reciprocal relation with q_{max} such that peak velocities less than $1/(q_{max}\Delta)$ cannot be resolved. Although zero-filling the $E(q)$ data before taking the Fourier transform increases the resolution, simple simulations show that the error associated with measuring the peak velocity is significantly greater than measuring the mean of the propagator. A more basic analysis of velocity uses the phase, θ, the angle between the real and imaginary channels, as a function of q with

$$\theta = q\langle v\rangle\Delta. \tag{6}$$

Using the difference between the phase (the phase shift) from multiple q-points subtracts phase offsets caused by factors other than coherent displacement [49, 50, 35, 51, 38, 39]. The most basic routine for measuring velocity in 1-D is a two q-point sampling strategy [51, 38]:

$$\langle v\rangle = \frac{\theta_2-\theta_1}{\Delta(q_2-q_1)}. \tag{7}$$

With at least 4 points, the method can be expanded to measure the 3-D velocity vector [14], and Pelc, et al., have developed and tested such sampling strategies [49].

3.2. Limits to flow detection with phase contrast velocimetry

We now derive the limit to flow detection and optimum q-space sampling strategy for phase contrast velocity. The limit to flow detection with Eq. (7) is equivalent to the limit associated with taking the mean of the propagator in the case that the propagator is symmetric about the mean displacement [24, 52].

When the limitation is viewed as the ability to resolve the signal phase shift above the noise floor, the signal-to-noise ratio (SNR $= I_0/\sigma_{noise}$) comes in. Fig. 1 shows the complex signal simulated from Eq. (1) with the addition of zero-mean

Gaussian noise such that SNR = 100. q is non-dimensionalized by the diffusive length scale such that $q* = q\sqrt{2D\Delta}$. Note 2π is not divided out, leaving $q*$ with units of radians. v is non-dimensionalized by Eq. (4) leading to $v* = v/\sqrt{2D/\Delta}$. With $v* = 0.01$, the imaginary signal is essentially zero. This is a characteristic of symmetric (zero-mean) propagators. At $v* = 0.1$, the imaginary signal is a visible sinusoid, indicating that this velocity can be resolved with SNR = 100. This is an order of magnitude less than $\langle v_{min}\rangle$ predicted by Eq. (4). With increasing velocity, the height of this lobe increases such that velocity can be measured in the presence of noise with increasing accuracy.

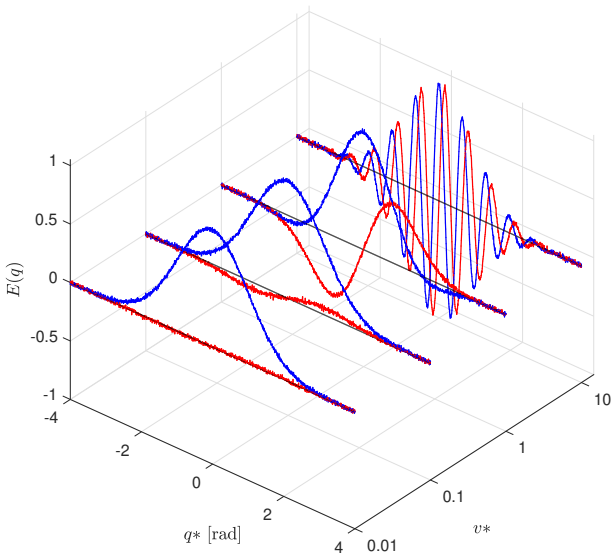

Figure 1: **Complex PGSE signal of fluid undergoing flow and diffusion.** Real (blue) and imaginary (red) signal simulated from Eq. (1) with SNR = 100 at variable velocities, non-dimensionalized by $q* = q\sqrt{2D\Delta}$ and $v* = v/\sqrt{2D/\Delta}$.

When $v* >> 1$, the sinusoidal nature of the real and imaginary signals is evident, reminiscent of a spin echo observed off-resonance, and the imaginary signal peaks at

$$q = \pm\pi(1 + 2N)/(2v\Delta), \tag{8}$$

with the first peak at $N = 0$. In the $v* >> 1$ regime, a 2-point phase contrast velocimetry sampling scheme requires $|q| < \pi/(v\Delta)$ in order to avoid Nyquist aliasing [53]. Therefore, some prior knowledge of the velocity is needed to optimize q-space sampling. However, when $v* < 1$, diffusive attenuation shifts the first lobe inwards and attenuates the signal before periodicity is observed at greater q. The imaginary signal is most resolved above a noise floor at the peaks of the first lobes, and thus this corresponding q value provides the greatest sensitivity to flow.

To find where the imaginary signal peaks in the case of $v* < 1$, we solve for q when the derivative with respect to q of the imaginary component of Eq. (1) is set to 0. From Euler's formula, the imaginary component is

$$Im(E(q)) = i\ \sin(qv\Delta)\exp(-q^2D\Delta). \tag{9}$$

Setting the first derivative to zero and rearranging terms, we get

$$\frac{v}{2qD} = \tan(qv\Delta) \approx qv\Delta, \tag{10}$$

with $qv\Delta$ being the first term in a Maclaurin series expansion of $\tan(q\Delta v)$. Therefore, for $v* << 1$, the imaginary component peaks at

$$q = \pm\frac{1}{\sqrt{2D\Delta}}. \tag{11}$$

Eq. (11) defines the optimum 2-point sampling strategy for velocimetry of slow flows and requires no prior knowledge of velocity. This q-value corresponds to an attenuation of $I(q)/I_0 = \exp(-1/2) \approx 0.6$.

As $v*$ decreases, the first lobe formed by the imaginary signal decreases and becomes less resolvable above a noise floor (Fig. (1)). The velocity at which the maximum imaginary signal is equal to σ_{noise} is the point at which the measured velocity is not statistically different from zero. This defines the slowest detectable velocity. The maximum imaginary signal is found by plugging Eq. (11) into Eq. (9). Setting this equal to 1/SNR and solving for $\langle v_{min}\rangle$ we get

$$\langle v_{min}\rangle = \sin^{-1}\left(\frac{\exp(1/2)}{\text{SNR}}\right)\sqrt{\frac{2D}{\Delta}}. \tag{12}$$

With $1/\text{SNR} << 1$, by a Maclaurin series expansion to first order,

$$\langle v_{min}\rangle \approx \frac{\exp(1/2)}{\text{SNR}}\sqrt{\frac{2D}{\Delta}}. \tag{13}$$

Compared to Eq. (4) and with typical SNR values, the rough value provided by Eq. (4) significantly overestimates $\langle v_{min}\rangle$. For instance, when SNR = 165, Eq. (4) overestimates $\langle v_{min}\rangle$ by a factor of 100.

The numerical solution to Eq. (10) for the location of the maximum of the first imaginary lobe in q-space is presented in Fig. 2a. The solution converges with Eq. (11) as $v*$ approaches zero, and converges with Eq. (8) when $v* >> 1$. The two limiting cases cross at $v* = \pi/2$. When $v* > \pi/2$, a fit of Eq. (6) to data found using the 2-point q-space sampling scheme based on Eq. (11) will encounter Nyquist aliasing issues.

Imaginary signals simulated from sampling q-points at the optimum value and the values for the limiting cases are compared in Fig. 2b. Imaginary signals cannot be distinguished from the noise when they decrease below 1/SNR. The imaginary signal at the peak of the first lobe normalized by I_0 is less than 10% different from the signal at $q = 1/\sqrt{2D\Delta}$ (Eq. (11)) when $v* = \pi/2$ and converges quickly for $v* < 1$. It is clear that Eq. (11) is valid for our purpose when $v* < \pi/2$. The equation for $\langle v_{min}\rangle$ (Eq. (13)) is rearranged and plotted as well, and shows good agreement for $Im(E(q))/I_0 << 1$, as anticipated. Basic understanding of PGSE NMR would lead one to think that larger q are needed to resolve slower flows. However, this thought can actually lead to completely missing the flow. Figure 2b shows that the imaginary signal from plugging Eq. (8) into Eq. (9) quickly approaches zero for $v* < 1$. At $v* = 1/2$, the imaginary signal is only 1% of I_0, thus hidden by the noise for SNR < 100.

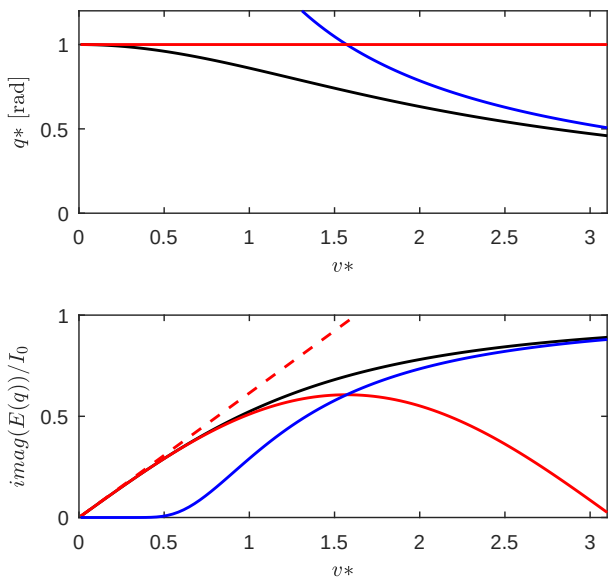

Figure 2: **Phase contrast velocimetry sampling strategies and detectability of slow flows.** a) Optimum q-space sampling for phase contrast velocimetry from Eq. (13) (black line), compared to the limiting cases for slow flows $v* << 1$ (Eq. (11), red line) and fast flows $v* >> 1$ (Eq. (8), blue line). The axes are non-dimensionalized, with $q* = q\sqrt{2D\Delta}$ and $v* = v/\sqrt{2D/\Delta}$. b) The imaginary signals at those q-point, normalized by I_0. The dotted red line is from Eq. (13), the first-order approximation of the solid red line.

4. Apparent diffusion/dispersion measurement

4.1. Background

Dispersion is the spreading of molecules that are initially adjacent in the flow path. Diffusion across shear fields, mechanical mixing due to tortuous flow paths around obstacles, and holdup of molecules in stagnant regions all cause dispersion. After molecules have sufficiently sampled the heterogeneity of the flow paths, the variance in molecular displacement is described by the asymptotic dispersion coefficient [5]. The measurement of dispersion with PGSE is well known in the porous media NMR community because it characterizes mass transport without the need for tracers and on length scales which are on the order of the pore size. PGSE experimental studies have been performed on model systems including Poiseuille pipe flow and flow through columns packed with monodisperse beads (bead packs) to better understand dispersive mass transport [5, 54, 55, 56, 57, 58, 59, 60, 61, 62, 63].

Some of the first diffusion MRI studies performed on human brains reported apparent diffusion coefficients (D_{app}) of tissue water which were higher than the self-diffusivity of water at body temperature [6, 64]. These studies attributed this paradoxical increase in D_{app} to tissue perfusion, in particular the microcirculation of blood in capillary networks, which produce additional intra-voxel incoherent motion (IVIM) in addition to the random Brownian motion of water molecules diffusing through the tissue. Although the flow paths of blood in the capillaries are separated such that the asymptotic dispersion coefficient cannot be reached, the D_{app} does still act as a measure of dispersive transport. Diffusion tensor imaging (DTI) methods have also been developed to assess cerebrospinal fluid motion along perivascular spaces [65, 3] (a key component of glymphatic clearance [66]). However, the IVIM and DTI literature and porous media literature have remained separate, with the medical PGSE MRI community only recently adopting the concept of dispersion [67].

Dispersion is measured from the PGSE signal attenuation. Flow sensitivity requires the capability to differentiate an apparent dispersion coefficient D^*_{app} as being greater than the apparent diffusion coefficient in the absence of flow. In porous materials and in the absence of flow, restrictions cause the apparent diffusion coefficient to decrease towards the tortuosity limit with increasing observation time, $\lim_{\Delta\to\infty} D_{app}(\Delta)/D_0 = D_\infty/D_0 = 1/\mathcal{T}$ [68]. The tortuosity depends on how well-connected the pores are. Simple obstructions imposed by the geometry of the porous media lead to D_∞/D_0 being primarily a function of ϵ, the liquid volume fraction (porosity) [69, 68, 70]. In contrast, with flow, the apparent dispersion coefficient increases and approaches the asymptotic dispersion coefficient, $\lim_{\Delta\to\infty} D^*_{app}(\Delta) = D^*$ [5]. The asymptotic dispersion limit can be unachievable in the PGSE observation time Δ because it requires that fluid molecules traverse distances long enough to average out effects of local heterogeneity [71, 60]. Therefore, although it may be impractical to reach the asymptotic limit, the greatest flow sensitivity is reached at an observation time which is as long as possible without experiencing significant signal loss from relaxation.

The dimensionless Péclet number is the ratio between advective and diffusive mass transport, and determines the importance of diffusion or advection in the stochastic spreading of solutes. The Péclet number is

$$Pé = \frac{\langle v\rangle l}{D_0} = \left(\frac{\epsilon}{1-\epsilon}\right)\frac{\langle v\rangle d_p}{D_0}, \tag{14}$$

where l is the characteristic length scale of the flow [72, 5]. $\langle v\rangle$ is the interstitial mean velocity, averaged only over the flowing liquid phase and the cross-sectional area taken up by that phase. The superficial velocity, the velocity of the flowing liquid phase averaged over the entire cross-sectional area is related to the interstitial velocity through $\langle v_s\rangle = \epsilon\,\langle v\rangle$. For a bead pack, l is related to the particle (bead) diameter by $l = \epsilon\, d_p/(1-\epsilon)$, leading to the second relation. Consistent with transport theory, for $Pé << 1$, PGSE measurements are sensitive only to diffusion. For $Pé >> 1$, D^*/D_0 scales with the Péclet number, $Pé = \langle v\rangle l/D_0$. The transition from Brownian motion to flow-enhanced dispersion which occurs when the dimensionless Péclet number increases above one ($Pé > 1$) was studied in the direction parallel to flow by Ding and Candela [54] and perpendicular to flow by Scheven [63].

4.2. Limits to flow detection with dispersion measurement

We are interested in the crossover from diffusive to dispersive transport which occurs near $Pé = 1$, since this is the point at which sensitivity to flow can be obtained. This also defines the lowest detectable flow from a measurement of D^*_{app}.

One case for which D^* can be modeled near $Pé = 1$ is fluid undergoing Poiseuille pipe flow. This is known as Taylor dispersion and occurs due to diffusion across a shear field causing

stochastic fluctuations in displacements along the direction of flow [73]. After fluid has sampled the shear field, such that $2D\Delta >> l$ where l is the radius of the pipe, the dispersion coefficient is [74, 71]

$$D^*/D_0 = 1 + \frac{l^2\langle v\rangle^2}{48D_0^2} = 1 + \frac{1}{48}Pé^2. \tag{15}$$

It is clear from the 1/48 prefactor and the squared dependence on $Pé$ that sensitivity to flow is negligible below $Pé = 1$. However, the prefactor is specific to the parabolic flow profile. Additionally, other dispersion mechanisms lead to a different scaling [72, 5]. For instance, mechanical dispersion from the tortuous flow paths of fluid flowing through a porous material scales linearly with $Pé$. Holdup dispersion due to regions of stagnant flow scales with $Pé \ln Pé$. These mechanisms can be envisioned in a biological context as well. For instance, Taylor dispersion of solutes in vascular blood flow, mechanical dispersion of solutes flowing through tissue along tortuous paths around cells, and holdup dispersion due to the many membranes and junctions which separate stagnant and flowing regions but are permeable and allow exchange of fluid components between the regions.

For fluid flow in porous media, dispersion occurs both in the direction parallel ($D^*_\parallel$) and perpendicular ($D^*_\perp$) to flow. Dispersion processes act differently in these directions [75]. Taylor dispersion acts perpendicular to local shear fields, which is predominantly parallel to the flow. Mechanical dispersion plays a large role for dispersion perpendicular to the flow. Dispersion is generally strongest in the direction of flow, and $D^*_\parallel \geq D^*_\perp$.

We experimentally investigated the crossover at $Pé = 1$ by measuring the dispersion coefficient of water flowing through a 5 mm flow column packed with 10 μm diameter polystyrene beads. This bead pack was used as a phantom of glymphatic flow through the brain interstitium, with the bead size chosen to approximate the cell size [67]. The bead pack porosity was $\epsilon = 0.367$, measured by the ratio between proton density images (using standard FLASH sequence) of water in beads and bulk water and agreeing with the ratio between $\langle v\rangle$ measured in the bulk and in the beadpack. MRI experiments were performed with an Avance III NMR spectrometer and a 7T magnet (Bruker BioSpin) with a bore temperature of 16.8 °C. Flow rates between 0 and 880 $\mu l/min$ were driven by a syringe pump (Harvard Apparatus) or a peristaltic pump (Pharmacia Biotec). A standard diffusion tensor imaging with echo planar imaging (DTI–EPI) sequence (Paravision 5.1, Bruker Biospin) was used with $\Delta/\delta = 50/3$ ms, gradients played out in 21 directions with $b-$values of 400 and 800 s/mm^2 and TE/TR=59/3000 ms. Two axial slices, through the bead pack and through a bulk fluid region above the bead pack, were obtained with 8 EPI segments, 2 mm slice thickness, 8 mm× 8 mm field of view with 0.125 mm× 0.125 mm in-plane resolution. SNR = 40 was calculated from the $b = 0$ image the intensity from an ROI in the bead pack as the signal and the standard deviation of an ROI outside of the column as the noise. $D_0 = 1.89$ m$^2/s$ was measured for bulk water outside the bead pack. The apparent dispersion coefficient was measured parallel ($D^*_\parallel$) and perpendicular ($D^*_\perp$) to the direction of flow from a region of interest which encompassed the cross-sectional area of the flow column. The diffusive length scale was larger than the bead diameter, $\sqrt{2Dt} > d_p$, such that D^*_{app} values were found (by varying Δ) to be near the asymptotic dispersion coefficient [67]. Results for $D^*_\parallel$ and $D^*_\perp$ are plotted in Figs. 3 and 4 on top of previous experimental results reproduced from Seymour and Callaghan [5].

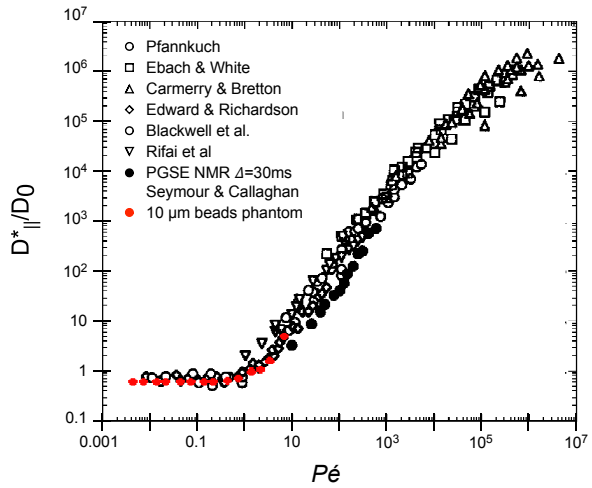

Figure 3: **Dispersion parallel to flow.** $D^*_\parallel$ measured in the range of $0.004 \leq Pé \leq 2$ (red), plotted on top of dispersion data from various experimental studies compiled by Seymour and Callaghan [5].

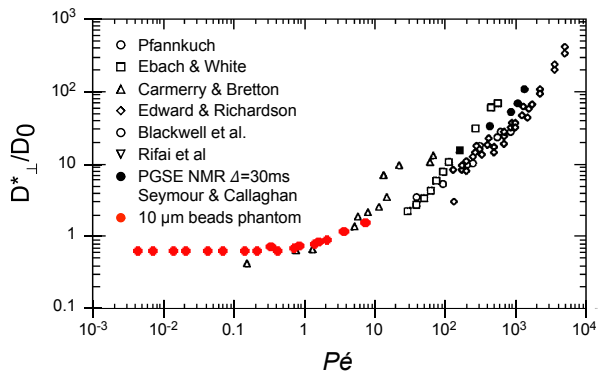

Figure 4: **Dispersion perpendicular to flow.** $D^*_\perp$ measured in the range of $0.004 \leq Pé \leq 2$ (red), plotted on top of dispersion data from various experimental studies compiled by Seymour and Callaghan [5].

With increasing flow rate, the first increase in D^* is seen at $Pé = 0.42$, at which point ($D^*_\parallel$) and ($D^*_\perp$) increased by 4% and 2%, respectively. At $Pé = 0.7$, the increase is more substantial with 16% and 8% respectively. Therefore, we find that flow can be detected with $Pé > 0.4$ at SNR = 40. $Pé$ is meant to be used as an order of magnitude analysis and there is no clear way to estimate l in non-ideal porous materials. Therefore, we simply stick to $Pé = 1$ as a rough estimate of the lowest detectable flow with dispersion. Through Eq. (14), this corresponds to

$$\langle v_{min}\rangle > \frac{l}{D_0}. \tag{16}$$

Additionally, as $D^*_{\parallel}$ increases more substantially than $D^*_{\perp}$, the fractional anisotropy from DTI may be applicable at detecting flow and its direction, as investigated by Komlosh *et al.* [67].

5. Discussion

5.1. How to best measure slow flows

Using stimulated echoes rather than spin echoes such that the maximum Δ is limited by T_1 rather than T_2 can be a strategy for resolving slow flows with phase contrast velocimetry [76, 77, 48]. However, with SNR being inversely related to $\langle v_{min} \rangle$, Δ must be increased by a factor of 4 to make up for half the signal being lost when using a stimulated echo. Therefore, roughly speaking, using stimulated echoes is a good strategy when $T_1 > 4T_2$. Magdoom *et al.* present and discuss a stimulated echo sequence as also being beneficial for overcoming phase error introduced by gradient hardware imperfections [48]. The measured dispersion coefficient can at most increase linearly with Δ, e.g., in the case of fluid in isolated capillaries which flow in opposite directions. In such a situation it could be beneficial to push Δ to as long as possible. However, in connected systems which are able to approach the asymptotic limit, there is marginal benefit to pushing Δ with the use of stimulated echoes. Minimizing signal loss is of greater concern.

A propagator approach is the most general means of measuring displacement. The component of a propagator which is symmetric about zero displacement can be subtracted from the total propagator to get at a propagator associated with fluid flowing in a preferential direction. This approach has been used to measure slow flows in plants [78]. However, the propagator requires a Fourier transform of data collected linearly with q and therefore requires a significant number of q-points. The mean apparent propagator (MAP) method was developed to reduce the data requirements of 3-D propagator measurements for clinical MRI, however it uses the magnitude data and therefore assumes that the propagator is symmetric [79, 80]. A generalized mean apparent propagator (GMAP) approach was developed to utilize the complex data and estimate asymmetric propagators and compared well with full propagator measurements on a bead pack flow phantom [81]. GMAP may be useful for isolating distinct flowing components directly from the propagator without linearly sampling q. At the same time, the limits to flow detection from the propagator rely on odd moments of the $E(q)$ data being visible. The odd moments are imaginary, as seen by an expansion of $E(q)$ in terms of the moments

$$E(q,\Delta) \approx 1 + iq \int_{-\infty}^{\infty} \overline{P}(Z,\Delta) Z dZ - \frac{1}{2} q^2 \int_{-\infty}^{\infty} \overline{P}(Z,\Delta) Z^2 dZ + \\ ... + \frac{1}{n!} i^n q^n \int_{-\infty}^{\infty} \overline{P}(Z,\Delta) Z^n dZ + ..., \quad (17)$$

and contribute to propagator asymmetry. The $1/n!$ prefactor shows that each subsequent moment contributes less significantly to the signal. The first two modes of the propagator are the mean and the variance, which are described by the $\langle v \rangle$ and D^*. Therefore, the limits to flow detection from a propagator measurement can be viewed as the same limits discussed for phase contrast and dispersion measurements. Additionally, for the purpose of detecting slow flows, experimental time may be better spent in acquiring fewer data points with higher SNR optimized for phase contrast and dispersion measurement than in acquiring the full propagator.

5.2. Limits to flow detection in vivo

We can derive useful approximations of low flow detection limits for *in vivo* imaging based on our derivations. With water $D_0 = 3 \times 10^{-9}\ m^2/s$ at $37°C$ [82], SNR = 100, and $\Delta = 1\ s$, the lowest detectable flow is $\langle v_{min} \rangle = 1\ \mu m/s$ with phase contrast velocimetry. This mean velocity must be coherent on the length scale of the voxel. With dispersion measurement, the lowest detectable velocity depends on a characteristic length scale for interstitial flow through tissue, which is ambiguous due to the heterogeneity of tissue. With a length scale of $l = 10\ \mu m$, which is roughly consistent with the diameter of cells, a minimum detectable mean velocity of $\langle v_{min} \rangle = 300\ \mu m/s$ with dispersion measurement is predicted. This does not need to be associated with flow which is coherent over the length scale of the voxel. These minimum detectable velocities should be compared to published values for the velocities associated with *in vivo* mass transport.

5.3. Applicability of PGSE MRI to imaging glymphatic clearance

The glymphatic system may play a critical role in prevention and recovery from neurodegenerative diseases and injuries. Currently, there is no clinical measure of glymphatic function. Dynamic contrast enhanced (DCE) MRI methods show promise [83], however intrathecal gadolinium contrast agent injection may be considered too invasive and risky in most cases. PGSE MRI has the potential to image glymphatic clearance without requiring exogeneous contrast agents. To assess applicability of PGSE MRI to imaging glymphatic clearance, we compare literature values for velocities associated with glympatic clearance (which were recently compiled in a review article [84]) to the minimum detectable velocities derived here. Note that there are very few experimentally measured velocities associated with glymphatic clearance (also highlighting the need for method development). With much unknown about the glymphatic system, the reported velocities are placeholders for future experimental findings. Therefore, the assessment of applicability is interpreted with an air of possibility.

In the glymphatic hypothesis, fluid moves into the brain along periarterial spaces, through the brain interstitium, and out of the brain along perivenous spaces [2]. Glymphatic clearance has been shown to increase during sleep [85]. DCE MRI measurements on live rat brains indicate diffusion and advection both contribute to interstitial transport [86] of the contrast agent. This and other research [87] suggests that the *Pé* of the contrast agent is in an intermediate regime (near 1), but that the *Pé* of water is less than 1. Finite element models were found to give the best comparison with real-time iontophoresis experiments of tetramethylammonium transport in brains of

anesthetized young adult mice when a superficial velocity of $\langle v_s \rangle = 10\ \mu m/s$ was included [87]. An upper bound for superficial velocity was estimated at $\langle v_s \rangle < 50\ \mu m/s$. The velocity was estimated $< 1\ \mu m/s$ during wakefulness. Since PGSE NMR is sensitive to both liquid inside and outside the cell, the superficial velocity is appropriate for comparison to $\langle v_{min} \rangle$. Measurement of interstitial flow with dispersion measurements may be possible if $\langle v_s \rangle$ was roughly an order of magnitude larger than is reported in Ref. [87]. Phase contrast velocimetry may be able to measure $\langle v_s \rangle = 10\ \mu m/s$ given high SNR and long Δ (e.g., SNR = 1000 and $\Delta = 1\ s$), and voxel sizes smaller than the distance between arterioles and venules, which has been measured at roughly 175 μm in mice [88] and 280 μm in primates [89].

Perivascular CSF flow is another point in the proposed mechanism of glymphatic clearance to which PGSE MRI might be sensitive. CSF in the annular spaces between vascular walls and astrocytic endfeet is connected to CSF in the subarachnoid space and the ventricles which bathes the brain [90, 91]. Tracer movement into the brain occurs along periarterial spaces faster than would be predicted by diffusion alone [92]. Pulsation of arterial walls with cardiac impulses causes motion of CSF [90, 66]. The glymphatic hypothesis is that there is peristaltic flow of CSF in the direction of blood flow and that the flow continues out of the brain on the perivenule side [2, 66]. Recent particle tracking velocimetry of fluorescent microspheres by two photon spectroscopy measure pulsatile flow of CSF in periarterial spaces of mice with velocities between $17-19\ \mu m/s$ in the direction of blood flow [93, 94]. These velocities are averaged over many cardiac cycles. The velocity profile was parabolic, as expected for laminar flow [93]. Microspheres were seen to oscillate back and forth $\Delta x = 14 \pm 2\mu m$ per cycle with approximately 360 bpm heart rate such that instantaneous velocities were greater than 100 $\mu m/s$ [94]. These velocities could be detectable with phase contrast velocimetry. Perivascular spaces were seen to be $l = 40\ \mu m$ wide [93]. Although such high resolution can be difficult to achieve *in vivo*, there are image processing approaches to enhance perivascular space visibility and quantification [95].

Although a constant flow of $17-19\ \mu m/s$ in a 40 μm channel would not lead to $Pé > 1$, additional mixing may occur in oscillatory flow due to the increased magnitude of the shear field. Enhancement of the dispersion coefficient of particles in fluid undergoing oscillatory flow in a pipe depend upon the Schmidt number $\mathrm{Sc} = \nu/D_0$, the Womersley number $\mathrm{Wo} = l(\omega\nu)^{1/2}$, and the dimensionless tidal displacement $\Delta x/l$ [96, 97]. Here, ν is the kinematic viscosity, ω is the angular frequency, and Δx is the amplitude of the displacements in oscillation. In perivascular spaces $\mathrm{Wo} << 1$, meaning that a parabolic flow profile has time to develop at any instant during the pulsation cycle, and $\mathrm{Sc} >> 1$. Leighton and McCready present a simplified equation for the enhancement of the dispersion coefficient in the limiting case that $\mathrm{Wo} \to 0$ and $\mathrm{Sc} \to \infty$, but where the product $\beta = \mathrm{Wo}/\mathrm{Sc}^{1/2} = (\omega l^2/D)^{1/2}$ is order one [98]. β can be thought of as the square root of the ratio between the timescale for particles to diffuse across the tube and the timescale of pulsation. From this equation, if particles diffuse across the tube much faster than the pulses are moving particles down the tube ($\beta < 1$) then there is no enhancement ($D^*/D_0 \approx 1$). If $\beta > 100$ then the enhancement is $D^*/D_0 \approx 1 + (\Delta x/l)^2$. The enhancement varies between these two extremes with a sigmoidal curve. Using parameters for periarterial flow in mice [93, 94], $l = 40\ \mu m$, $\omega = 2\pi \times 360$, and $D_0 = 3 \times 10^{-9}\ m^2/s$, yields $\beta = 35$, corresponding to an enhancement of roughly $D^*/D_0 = 1 + 0.9(\Delta x/l)^2$. With $\Delta x/l = 14/40 = 0.35$, the enhancement is $D^*/D_0 = 1.1$. It appears that periarterial flow may be in an intermediate regime where enhanced dispersion may be measurable under ideal conditions. Note that there are reports of using DTI to measure periarterial flow as a means of assessing glymphatic clearance [7, 99, 8]. Additionally, note that the enhancement is a function of $(\Delta x/l)^2$. The amplitude of CSF pulsations in ventricles of human volunteers was seen to increase significantly during non-rapid eye movement sleep relative to during wakefulness [100]. These waves of CSF inflow could increase Δx significantly, enhancing dispersion along periarterial spaces during sleep. One challenge which must be considered is the timescale of observation (Δ) relative to the timescale of pulsation. Since $\Delta \lessapprox 1/\omega$, PGSE will not measure the asymptotic dispersion tensor. For maximal sensitivity, diffusion should be encoded when the amplitude of the flow is greatest. With hemodynamics and cerebrospinal fluid oscillations being coupled, it may be possible use cardiac gating to trigger each scan to start with a CSF impulse [100].

6. Conclusion

Displacements due to flow become difficult to detect when they are similar or less than diffusive displacements. We provide theory and equations for the lowest detectable velocities from the phase shift (phase contrast velocimetry) and the attenuation (apparent diffusion/dispersion measurement) of PGSE signal. The equations for phase contrast velocimetry predict minimum velocities over an order of magnitude less than the previously accepted estimate. A q-space sampling strategy is presented for phase contrast velocimetry in the low flow regime which requires no prior knowledge of the velocity. Concepts of dispersion from porous media NMR are used to show that the lowest detectable velocity is a function of the Péclet number. We experimentally validate this for dispersion parallel and perpendicular to flow in a bead pack. The lowest detectable velocities *in vivo* are discussed and compared to literature values for velocities associated with glymphatic clearance.

Acknowledgements

NHW was funded by the NIGMS PRAT fellowship Award # FI2GM133445-01. PJB was supported by the IRP of the NICHD, NIH. DB and MK were supported by the Center for Neuroscience and Regenerative Medicine, Henry Jackson Foundation, Bethesda, MD. NHW is grateful for mentorship from Joe Seymour and Sarah Codd.

References

[1] E. Stejskal, Use of spin echoes in a pulsed magnetic-field gradient to study anisotropic, restricted diffusion and flow, The Journal of Chemical Physics 43 (10) (1965) 3597–3603 (1965).

[2] J. J. Iliff, M. Wang, Y. Liao, B. A. Plogg, W. Peng, G. A. Gundersen, H. Benveniste, G. E. Vates, R. Deane, S. A. Goldman, et al., A paravascular pathway facilitates csf flow through the brain parenchyma and the clearance of interstitial solutes, including amyloid β, Science translational medicine 4 (147) (2012) 147ra111–147ra111 (2012).

[3] I. F. Harrison, B. Siow, A. B. Akilo, P. G. Evans, O. Ismail, Y. Ohene, P. Nahavandi, D. L. Thomas, M. F. Lythgoe, J. A. Wells, Non-invasive imaging of csf-mediated brain clearance pathways via assessment of perivascular fluid movement with diffusion tensor mri, Elife 7 (2018) e34028 (2018).

[4] P. T. Callaghan, Principles of nuclear magnetic resonance microscopy, Clarendon Press, Oxford, 1991 (1991).

[5] J. D. Seymour, P. T. Callaghan, Generalized approach to nmr analysis of flow and dispersion in porous media, AIChE Journal 43 (8) (1997) 2096–2111 (1997).

[6] D. Le Bihan, E. Breton, D. Lallemand, P. Grenier, E. Cabanis, M. Laval-Jeantet, Mr imaging of intravoxel incoherent motions: application to diffusion and perfusion in neurologic disorders., Radiology 161 (2) (1986) 401–407 (1986).

[7] B. A. Plog, M. Nedergaard, The glymphatic system in central nervous system health and disease: Past, present, and future, Annual Review of Pathology: Mechanisms of Disease (0) (2017).

[8] T. Taoka, S. Naganawa, Glymphatic imaging using mri, Journal of Magnetic Resonance Imaging 51 (1) (2020) 11–24 (2020).

[9] F. Bloch, Nuclear induction, Physical Review 70 (7-8) (1946) 460 (1946).

[10] H. C. Torrey, Bloch equations with diffusion terms, Physical Review 104 (1956) 563–565 (Nov 1956). doi:10.1103/PhysRev.104.563.

[11] E. Stejskal, J. Tanner, Spin diffusion measurements: Spin echoes in the presence of a time-dependent field gradient, The Journal of Chemical Physics 42 (1962) 288–298 (1962).

[12] The propagator representation of molecular transport in microporous crystallites, Journal of Magnetic Resonance 51 (1) (1983) 1 – 7 (1983). doi:https://doi.org/10.1016/0022-2364(83)90094-X.

[13] H. Y. Carr, E. M. Purcell, Effects of diffusion on free precession in nuclear magnetic resonance experiments, Physical review 94 (3) (1954) 630 (1954).

[14] C. Dumoulin, S. Souza, M. Walker, W. Wagle, Three-dimensional phase contrast angiography, Magnetic Resonance in Medicine 9 (1) (1989) 139–149 (1989).

[15] C. Jenner, Y. Xia, C. Eccles, P. Callaghan, Circulation of water within wheat grain revealed by nuclear magnetic resonance micro-imaging, Nature 336 (6197) (1988) 399 (1988).

[16] W. Köckenberger, J. Pope, Y. Xia, K. Jeffrey, E. Komor, P. Callaghan, A non-invasive measurement of phloem and xylem water flow in castor bean seedlings by nuclear magnetic resonance microimaging, Planta 201 (1) (1997) 53–63 (1997).

[17] M. Rokitta, U. Zimmermann, A. Haase, Fast nmr flow measurements in plants using flash imaging, Journal of Magnetic Resonance 137 (1) (1999) 29–32 (1999).

[18] A. Peuke, M. Rokitta, U. Zimmermann, L. Schreiber, A. Haase, Simultaneous measurement of water flow velocity and solute transport in xylem and phloem of adult plants of ricinus communis over a daily time course by nuclear magnetic resonance spectrometry, Plant, Cell & Environment 24 (5) (2001) 491–503 (2001).

[19] J.-W. van de Meent, A. J. Sederman, L. F. Gladden, R. E. Goldstein, Measurement of cytoplasmic streaming in single plant cells by magnetic resonance velocimetry, Journal of Fluid Mechanics 642 (2010) 5–14 (2010).

[20] C. W. Windt, P. Blümler, A portable nmr sensor to measure dynamic changes in the amount of water in living stems or fruit and its potential to measure sap flow, Tree Physiology 35 (4) (2015) 366–375 (2015). doi:10.1093/treephys/tpu105.

[21] Development of an outdoor mri system for measuring flow in a living tree, Journal of Magnetic Resonance 265 (2016) 129 – 138 (2016). doi:https://doi.org/10.1016/j.jmr.2016.02.004.

[22] Nmr velocimetry with 13-interval stimulated echo multi-slice imaging in natural porous media under low flow rates, Journal of Magnetic Resonance 212 (1) (2011) 216 – 223 (2011). doi:https://doi.org/10.1016/j.jmr.2011.07.004.

[23] Velocity distribution of slow fluid flows in bentheimer sandstone: An nmri and propagator study, Magnetic Resonance Imaging 14 (9) (1996) 1085 – 1091 (1996). doi:https://doi.org/10.1016/S0730-725X(96)00110-5.

[24] Accurate phase-shift velocimetry in rock, Journal of Magnetic Resonance 267 (2016) 43 – 53 (2016). doi:https://doi.org/10.1016/j.jmr.2016.04.006.

[25] B. S. Akpa, S. M. Matthews, A. J. Sederman, K. Yunus, A. C. Fisher, M. L. Johns, L. F. Gladden, Study of miscible and immiscible flows in a microchannel using magnetic resonance imaging, Analytical Chemistry 79 (16) (2007) 6128–6134, pMID: 17630718 (2007). doi:10.1021/ac070364a.

[26] J. Zhang, B. J. Balcom, Parallel-plate rf resonator imaging of chemical shift resolved capillary flow, Magnetic resonance imaging 28 (6) (2010) 826–833 (2010).

[27] S. Ahola, V.-V. Telkki, S. Stapf, Velocity distributions in a micromixer measured by nmr imaging, Lab on a Chip 12 (10) (2012) 1823–1830 (2012).

[28] 3d mri velocimetry of non-transparent 3d-printed staggered herringbone mixers, Chemical Engineering Journal 343 (2018) 54 – 60 (2018). doi:https://doi.org/10.1016/j.cej.2018.02.096.

[29] U. Tallarek, D. Van Dusschoten, H. Van As, E. Bayer, G. Guiochon, Study of transport phenomena in chromatographic columns by pulsed field gradient nmr, The Journal of Physical Chemistry B 102 (18) (1998) 3486–3497 (1998).

[30] J. Park, S. J. Gibbs, Mapping flow and dispersion in a packed column by mri, AIChE Journal 45 (3) 655–660. doi:10.1002/aic.690450322.

[31] Adapted mr velocimetry of slow liquid flow in porous media, Journal of Magnetic Resonance 276 (2017) 103 – 112 (2017). doi:https://doi.org/10.1016/j.jmr.2017.01.017.

[32] Colloid deposition in monolithic porous media – experimental investigations using x-ray computed microtomography and magnetic resonance velocimetry, Chemical Engineering Science 175 (2018) 257 – 266 (2018). doi:https://doi.org/10.1016/j.ces.2017.09.054.

[33] Nuclear magnetic resonance microscopy studies of membrane biofouling, Journal of Membrane Science 323 (1) (2008) 37 – 44 (2008). doi:https://doi.org/10.1016/j.memsci.2008.06.012.

[34] L. Gladden, M. Lim, M. Mantle, A. Sederman, E. Stitt, Mri visualisation of two-phase flow in structured supports and trickle-bed reactors, Catalysis Today 79 (2003) 203–210 (2003).

[35] P. R. Moran, A flow velocity zeugmatographic interlace for nmr imaging in humans, Magnetic resonance imaging 1 (4) (1982) 197–203 (1982).

[36] N. J. Pelc, R. J. Herfkens, A. Shimakawa, Enzmann, D. R, Phase contrast cine magnetic resonance imaging, Magnetic resonance quarterly 7 (4) (1991) 229–254 (1991).

[37] M. Marks, N. Pelc, M. Ross, D. Enzmann, Determination of cerebral blood flow with a phase-contrast cine mr imaging technique: evaluation of normal subjects and patients with arteriovenous malformations., Radiology 182 (2) (1992) 467–476 (1992).

[38] M. O'donnell, Nmr blood flow imaging using multiecho, phase contrast sequences, Medical physics 12 (1) (1985) 59–64 (1985).

[39] G. Nayler, D. Firmin, D. Longmore, et al., Blood flow imaging by cine magnetic resonance, J Comput Assist Tomogr 10 (5) (1986) 715–722 (1986).

[40] M. C. Dulce, G. H. Mostbeck, M. O'Sullivan, M. Cheitlin, G. R. Caputo, C. B. Higgins, Severity of aortic regurgitation: interstudy reproducibility of measurements with velocity-encoded cine mr imaging., Radiology 185 (1) (1992) 235–240 (1992).

[41] J.-P. E. Kvitting, T. Ebbers, L. Wigström, J. Engvall, C. L. Olin, A. F. Bolger, Flow patterns in the aortic root and the aorta studied with time-resolved, 3-dimensional, phase-contrast magnetic resonance imaging: implications for aortic valve–sparing surgery, The Journal of Thoracic and Cardiovascular Surgery 127 (6) (2004) 1602 – 1607 (2004). doi:https://doi.org/10.1016/j.jtcvs.2003.10.042.
URL `http://www.sciencedirect.com/science/article/pii/S002252230`

[42] A. Frydrychowicz, M. Markl, D. Hirtler, A. Harloff, C. Schlensak, J. Geiger, B. Stiller, R. Arnold, Aortic hemodynamics in patients with

and without repair of aortic coarctation: in vivo analysis by 4d flow-sensitive magnetic resonance imaging, Investigative radiology 46 (5) (2011) 317–325 (2011).

[43] D. Enzmann, N. Pelc, Normal flow patterns of intracranial and spinal cerebrospinal fluid defined with phase-contrast cine mr imaging., Radiology 178 (2) (1991) 467–474 (1991).

[44] D. R. Enzmann, N. J. Pelc, Cerebrospinal fluid flow measured by phase-contrast cine mr, American journal of neuroradiology 14 (6) (1993) 1301–1307 (1993).

[45] A pgse study of propane gas flow through model porous bead packs, Journal of Magnetic Resonance 163 (1) (2003) 16 – 22 (2003). doi:https://doi.org/10.1016/S1090-7807(03)00111-3.

[46] Nanoscale nmr velocimetry by means of slowly diffusing tracer particles, Journal of Magnetic Resonance 169 (2) (2004) 250 – 256 (2004). doi:https://doi.org/10.1016/j.jmr.2004.05.005.

[47] E. O. Fridjonsson, J. D. Seymour, S. L. Codd, Anomalous preasymptotic colloid transport by hydrodynamic dispersion in microfluidic capillary flow, Phys. Rev. E 90 (2014) 010301 (Jul 2014). doi:10.1103/PhysRevE.90.010301.

[48] K. N. Magdoom, A. Zeinomar, R. R. Lonser, M. Sarntinoranont, T. H. Mareci, Phase contrast mri of creeping flows using stimulated echo, Journal of Magnetic Resonance 299 (2019) 49–58 (2019).

[49] N. J. Pelc, M. A. Bernstein, A. Shimakawa, G. H. Glover, Encoding strategies for three-direction phase-contrast mr imaging of flow, Journal of Magnetic Resonance Imaging 1 (4) (1991) 405–413 (1991).

[50] T. Grover, J. Singer, Nmr spin-echo flow measurements, Journal of Applied Physics 42 (3) (1971) 938–940 (1971).

[51] D. A. Feinberg, L. E. Crooks, P. Sheldon, J. H. Iii, J. Watts, M. Arakawa, Magnetic resonance imaging the velocity vector components of fluid flow, Magnetic resonance in medicine 2 (6) (1985) 555–566 (1985).

[52] A. Vallatos, H. F. Al-Mubarak, J. M. Mullin, W. M. Holmes, Accuracy of phase-contrast velocimetry in systems with skewed intravoxel velocity distributions, Journal of Magnetic Resonance 296 (2018) 121–129 (2018).

[53] C. J. Elkins, M. T. Alley, Magnetic resonance velocimetry: applications of magnetic resonance imaging in the measurement of fluid motion, Experiments in Fluids 43 (6) (2007) 823–858 (2007).

[54] A. Ding, D. Candela, Probing nonlocal tracer dispersion in flows through random porous media, Physical Review E 54 (1) (1996) 656 (1996).

[55] L. Lebon, L. Oger, J. Leblond, J. Hulin, N. Martys, L. Schwartz, Pulsed gradient nmr measurements and numerical simulation of flow velocity distribution in sphere packings, Physics of Fluids 8 (2) (1996) 293–301 (1996).

[56] S. L. Codd, B. Manz, J. D. Seymour, P. T. Callaghan, Taylor dispersion and molecular displacements in poiseuille flow, Phys. Rev. E 60 (1999) R3491–R3494 (Oct 1999). doi:10.1103/PhysRevE.60.R3491.

[57] S. Stapf, K. Packer, R. Graham, J.-F. Thovert, P. Adler, Spatial correlations and dispersion for fluid transport through packed glass beads studied by pulsed field-gradient nmr, Physical Review E 58 (5) (1998) 6206 (1998).

[58] D. Kandhai, D. Hlushkou, A. G. Hoekstra, P. M. Sloot, H. Van As, U. Tallarek, Influence of stagnant zones on transient and asymptotic dispersion in macroscopically homogeneous porous media, Physical review letters 88 (23) (2002) 234501 (2002).

[59] U. M. Scheven, P. N. Sen, Spatial and temporal coarse graining for dispersion in randomly packed spheres, Physical review letters 89 (25) (2002) 254501 (2002).

[60] A. Khrapitchev, P. Callaghan, Reversible and irreversible dispersion in a porous medium, Physics of Fluids 15 (9) (2003) 2649–2660 (2003).

[61] U. Scheven, R. Harris, M. Johns, Intrinsic dispersivity of randomly packed monodisperse spheres, Physical review letters 99 (5) (2007) 054502 (2007).

[62] M. Hunter, P. Callaghan, Nmr measurement of nonlocal dispersion in complex flows, Physical review letters 99 (21) (2007) 210602 (2007).

[63] U. Scheven, Pore-scale mixing and transverse dispersivity of randomly packed monodisperse spheres, Physical review letters 110 (21) (2013) 214504 (2013).

[64] D. Le Bihan, E. Breton, D. Lallemand, M. Aubin, J. Vignaud, M. Laval-Jeantet, Separation of diffusion and perfusion in intravoxel incoherent motion mr imaging., Radiology 168 (2) (1988) 497–505 (1988).

[65] T. Taoka, Y. Masutani, H. Kawai, T. Nakane, K. Matsuoka, F. Yasuno, T. Kishimoto, S. Naganawa, Evaluation of glymphatic system activity with the diffusion mr technique: diffusion tensor image analysis along the perivascular space (dti-alps) in alzheimer's disease cases, Japanese journal of radiology 35 (4) (2017) 172–178 (2017).

[66] J. J. Iliff, M. Wang, D. M. Zeppenfeld, A. Venkataraman, B. A. Plog, Y. Liao, R. Deane, M. Nedergaard, Cerebral arterial pulsation drives paravascular csf–interstitial fluid exchange in the murine brain, Journal of Neuroscience 33 (46) (2013) 18190–18199 (2013).

[67] M. E. Komlosh, D. Benjamini, N. Williamson, F. Horkay, E. B. Hutchinson, P. J. Basser, A novel mri phantom to study interstitial fluid transport in the glymphatic system, Magnetic resonance imaging 56 (2019) 181–186 (2019).

[68] L. Latour, R. L. Kleinberg, P. P. Mitra, C. H. Sotak, Pore-size distributions and tortuosity in heterogeneous porous media, Journal of Magnetic Resonance, Series A 112 (1) (1995) 83–91 (1995).

[69] K. Fukuda, T. Kasuga, T. Mizusaki, A. Hirai, K. Eguchi, Study of self-diffusion process of water molecules in porous glass by stimulated spin echo method with pulsed field gradients, Journal of the Physical Society of Japan 58 (5) (1989) 1662–1666 (1989).

[70] L. L. Latour, K. Svoboda, P. P. Mitra, C. H. Sotak, Time-dependent diffusion of water in a biological model system., Proceedings of the National Academy of Sciences 91 (4) (1994) 1229–1233 (1994).

[71] P. Callaghan, S. Codd, J. Seymour, Spatial coherence phenomena arising from translational spin motion in gradient spin echo experiments, Concepts in Magnetic Resonance 11 (4) (1999) 181–202 (1999).

[72] O. Plumb, S. Whitaker, Diffusion, adsorption and dispersion in porous media: small-scale averaging and local volume averaging, IN: Dynamics of Fluids in Hierarchical Porous Media. Academic Press, Inc., San Diego, California. 1990. p 97-148, 13 fig, 58 ref. (1990).

[73] Dispersion of soluble matter in solvent flowing slowly through a tube 219 (1137) (1953) 186–203 (1953). doi:10.1098/rspa.1953.0139.

[74] R. Aris, On the dispersion of a solute in a fluid flowing through a tube, Proceedings of the Royal Society of London. Series A. Mathematical and Physical Sciences 235 (1200) (1956) 67–77 (1956).

[75] B. Manz, P. Alexander, L. Gladden, Correlations between dispersion and structure in porous media probed by nuclear magnetic resonance, Physics of Fluids 11 (2) (1999) 259–267 (1999).

[76] D. Bourgeois, M. Decorps, Quantitative imaging of slow coherent motion by stimulated echoes with suppression of stationary water signal, Journal of Magnetic Resonance (1969) 94 (1) (1991) 20–33 (1991).

[77] T. Scheenen, F. Vergeldt, C. Windt, P. De Jager, H. Van As, Microscopic imaging of slow flow and diffusion: a pulsed field gradient stimulated echo sequence combined with turbo spin echo imaging, Journal of Magnetic Resonance 151 (1) (2001) 94–100 (2001).

[78] C. W. Windt, F. J. Vergeldt, P. A. De Jager, H. Van As, Mri of long-distance water transport: a comparison of the phloem and xylem flow characteristics and dynamics in poplar, castor bean, tomato and tobacco, Plant, Cell & Environment 29 (9) (2006) 1715–1729 (2006).

[79] E. Özarslan, C. G. Koay, T. M. Shepherd, M. E. Komlosh, M. O. İrfanoğlu, C. Pierpaoli, P. J. Basser, Mean apparent propagator (map) mri: a novel diffusion imaging method for mapping tissue microstructure, NeuroImage 78 (2013) 16–32 (2013).

[80] A. V. Avram, J. E. Sarlls, A. S. Barnett, E. Özarslan, C. Thomas, M. O. Irfanoglu, E. Hutchinson, C. Pierpaoli, P. J. Basser, Clinical feasibility of using mean apparent propagator (map) mri to characterize brain tissue microstructure, NeuroImage 127 (2016) 422–434 (2016).

[81] D. Benjamini, M. E. Komlosh, N. H. Williamson, P. J. Basser, Generalized mean apparent propagator mri to measure and image advective and dispersive flows in medicine and biology, IEEE transactions on medical imaging 38 (1) (2018) 11–20 (2018).

[82] R. Mills, Self-diffusion in normal and heavy water in the range 1-45. deg., The Journal of Physical Chemistry 77 (5) (1973) 685–688 (1973).

[83] H. Lee, K. Mortensen, S. Sanggaard, P. Koch, H. Brunner, B. Quistorff, M. Nedergaard, H. Benveniste, Quantitative gd-dota uptake from cerebrospinal fluid into rat brain using 3d vfa-spgr at 9.4 t, Magnetic resonance in medicine 79 (3) (2018) 1568–1578 (2018).

[84] L. A. Ray, J. J. Heys, Fluid flow and mass transport in brain tissue, Fluids 4 (4) (2019) 196 (2019).

[85] L. Xie, H. Kang, Q. Xu, M. J. Chen, Y. Liao, M. Thiyagarajan, J. O'Donnell, D. J. Christensen, C. Nicholson, J. J. Iliff, et al., Sleep drives metabolite clearance from the adult brain, science 342 (6156)

(2013) 373–377 (2013).
[86] S. Koundal, R. Elkin, S. Nadeem, Y. Xue, S. Constantinou, S. Sanggaard, X. Liu, B. Monte, F. Xu, W. Van Nostrand, et al., Glymphatic optimal mass transport with lagrangian workflow reveals advective and diffusion driven solute transport, bioRxiv (2019) 765370 (2019).
[87] L. Ray, J. J. Iliff, J. J. Heys, Analysis of convective and diffusive transport in the brain interstitium, Fluids and Barriers of the CNS 16 (1) (2019) 6 (2019).
[88] N. Nishimura, C. B. Schaffer, B. Friedman, P. D. Lyden, D. Kleinfeld, Penetrating arterioles are a bottleneck in the perfusion of neocortex, Proceedings of the National Academy of Sciences 104 (1) (2007) 365–370 (2007).
[89] D. L. Adams, V. Piserchia, J. R. Economides, J. C. Horton, Vascular supply of the cerebral cortex is specialized for cell layers but not columns, Cerebral Cortex 25 (10) (2014) 3673–3681 (2014).
[90] M. L. Rennels, T. F. Gregory, O. R. Blaumanis, K. Fujimoto, P. A. Grady, Evidence for a 'paravascular' fluid circulation in the mammalian central nervous system, provided by the rapid distribution of tracer protein throughout the brain from the subarachnoid space, Brain research 326 (1) (1985) 47–63 (1985).
[91] K. N. Magdoom, A. Brown, J. Rey, T. H. Mareci, M. A. King, M. Sarntinoranont, Mri of whole rat brain perivascular network reveals role for ventricles in brain waste clearance, Scientific reports 9 (1) (2019) 1–11 (2019).
[92] H. F. Cserr, L. Ostrach, Bulk flow of interstitial fluid after intracranial injection of blue dextran 2000, Experimental neurology 45 (1) (1974) 50–60 (1974).
[93] H. Mestre, J. Tithof, T. Du, W. Song, W. Peng, A. M. Sweeney, G. Olveda, J. H. Thomas, M. Nedergaard, D. H. Kelley, Flow of cerebrospinal fluid is driven by arterial pulsations and is reduced in hypertension, Nature communications 9 (1) (2018) 4878 (2018).
[94] B. Bedussi, M. Almasian, J. de Vos, E. VanBavel, E. N. Bakker, Paravascular spaces at the brain surface: Low resistance pathways for cerebrospinal fluid flow, Journal of Cerebral Blood Flow & Metabolism 38 (4) (2018) 719–726 (2018).
[95] F. Sepehrband, G. Barisano, N. Sheikh-Bahaei, R. P. Cabeen, J. Choupan, M. Law, A. W. Toga, Image processing approaches to enhance perivascular space visibility and quantification using mri, Scientific reports 9 (1) (2019) 1–12 (2019).
[96] E. Watson, Diffusion in oscillatory pipe flow, Journal of Fluid Mechanics 133 (1983) 233–244 (1983).
[97] C. Joshi, R. Kamm, J. Drazen, A. Slutsky, An experimental study of gas exchange in laminar oscillatory flow, Journal of Fluid Mechanics 133 (1983) 245–254 (1983).
[98] D. T. Leighton, M. J. McCready, Shear enhanced transport in oscillatory liquid membranes, AIChE journal 34 (10) (1988) 1709–1712 (1988).
[99] F. Sepehrband, R. P. Cabeen, J. Choupan, G. Barisano, M. Law, A. W. Toga, A. D. N. Initiative, et al., Perivascular space fluid contributes to diffusion tensor imaging changes in white matter, NeuroImage 197 (2019) 243–254 (2019).
[100] N. E. Fultz, G. Bonmassar, K. Setsompop, R. A. Stickgold, B. R. Rosen, J. R. Polimeni, L. D. Lewis, Coupled electrophysiological, hemodynamic, and cerebrospinal fluid oscillations in human sleep, Science 366 (6465) (2019) 628–631 (2019).